1 This paper is a non-peer-reviewed preprint submitted to EarthArXiv.

submitted to *Geophys. J. Int.*

Spatiotemporal forecast of extreme events in a chaotic dynamical model of slow slip events

Hojjat Kaveh[1⋆], Jean Philippe Avouac[2], Andrew M Stuart [3]

[1] *Mechanical and Civil Engineering, California Institute of Technology, Pasadena, CA, USA*

[2] *Geology and Planetary Science, California Institute of Technology, Pasadena, CA, USA*

[3] *Computing and Mathematical Science, California Institute of Technology, Pasadena, CA, USA*

SUMMARY

Seismic and aseismic slip events result from episodic slips on faults and are often chaotic due to stress heterogeneity. Their predictability in nature is a widely open question. In this study, we forecast extreme events in a numerical model. The model, which consists of a single fault governed by rate-and-state friction, produces realistic sequences of slow events with a wide range of magnitudes and inter-event times. The complex dynamics of this system arise from partial ruptures. As the system self-organizes, prestress is confined to a chaotic attractor of a relatively small dimension. We identify the instability regions within this attractor where large events initiate. These regions correspond to the particular stress distributions that are favorable for near complete ruptures of the fault. We show that large events can be forecasted in time and space based on the determination of these instability regions in a low-dimensional space and the knowledge of the current slip rate on the fault.

Key words:

Seismic cycle – Self-organization – Earthquake interaction, forecasting, and prediction –Numerical modelling

⋆ orresponding author; E-mail: hkaveh@caltech.edu.

1 INTRODUCTION

Earthquakes and Slow Slip Events (SSEs) result from episodic frictional slip on the faults. Each slip event releases the elastic strain accumulated during an interevent period during which the fault is locked. This principle is often referred to as the elastic rebound theory in reference to Reid (1910). While the elastic rebound theory offers valuable insights into the long-term mean recurrence time of earthquakes and can be used for time-independent earthquake forecasting (Avouac, 2015; Marsan & Tan, 2020), it falls short of predicting the time or the magnitude of the larger events (Murray & Segall, 2002). The difficulty is that earthquakes often exhibit a chaotic behavior which is manifest in the irregular and rare occurrence of large slip events and various empirical scaling laws, such as the Gutenberg-Richter and the Omori laws (Scholz, 1989). The Gutenberg-Richter law (Gutenberg & Richter, 1950) states that earthquake magnitudes are distributed exponentially (the number of earthquakes with magnitude larger than M, $N(M)$, is given by $\log_{10} N(M) = a - bM$, where b is a scaling parameter of the order of one and a is a constant). The Omori law (Utsu et al., 1995) states that the rate of earthquakes during an aftershock sequence decays as $1/t$ where t is the time since the mainshock. Chaotic behavior has also been identified in sequences of SSEs in Cascadia (Gualandi et al., 2020). These events obey the same scaling laws as regular earthquakes and produce very similar crack-like and pulse-like ruptures, although with several orders of magnitudes smaller slip rate and stress drop (Michel et al., 2019).

The main source of complexities in earthquake sequences is due to stress heterogeneities which can either be of static origin (due to faults geometry (Okubo & Aki, 1987), roughness (Sagy et al., 2007; Cattania, 2019), or heterogeneity of mechanical properties (Kaneko et al., 2010)) or dynamic, due stress transfers among faults or within a single fault (Shaw & Rice, 2000). As the stress evolves during the earthquake cycle, it generates asperities and barriers that can either facilitate a complete rupture of a fault (a system-size rupture) or impede the propagation of a rupture, resulting in a partial rupture. Partial or complete ruptures of a fault system are therefore observed in nature (Konca et al., 2008). Large ruptures, though rare according to the Gutenberg-Richter law, hold greater significance from a seismic hazard perspective.

Advances in the understanding of fault friction (Marone, 1998) and in numerical modeling of earthquake sequences (Rice, 1993; Lapusta et al., 2000; Lapusta & Liu, 2009) now make it possible to produce realistic simulations (Barbot et al., 2012). When performing those numerical simulations, initial conditions cannot be any arbitrary value, and it is also crucial to recognize that certain initial conditions hold more statistical relevance than others during the evolution of the dynamical system. For example, Lapusta & Rice (2003) and Rubin & Ampuero (2005) advocate for conducting simulations over multiple seismic cycles to mitigate the influence of arbitrary choices in initial conditions. In fact, the space of feasible stress distributions on a fault during earthquake cycles is significantly smaller than the space of arbitrary initial conditions, as the dynamical system self-organizes into a chaotic attractor (Shaw & Rice, 2000). When a dynamical system converges to its chaotic attractor, any state outside this attractor is not feasible within the system's evolution. Consequently, the space of feasible states is limited to the attractor itself, resulting in a significantly smaller domain compared to the space of any arbitrary states for the system.

Large events happen rarely in the chaotic evolution of the earthquake cycle so their forecast is extremely challenging. We hypothesize that as for other types of dynamical systems that produce extreme (or rare) events (Blonigan et al., 2019; Farazmand & Sapsis, 2019), the trajectory of the dynamical system must traverse specific instability regions within the chaotic attractor for large fault ruptures to occur. These instability regions correspond to the optimal distributions of stress (or the states of the frictional interface) that facilitate large ruptures and are also accessible during the evolution of the system because they are part of the chaotic attractor. Despite considerable research on deterministic chaos in earthquake cycle models (Huang & Turcotte, 1990; Becker, 2000; Anghel et al., 2004; Kato, 2016; Barbot, 2019), certain essential features of the chaotic attractor, particularly modes relevant to instability that are also statistically feasible, have remained elusive in the literature. This is primarily due to the high-dimensional, chaotic, and multi-scale nature of the problem, as well as the rarity of large events.

The identification of the optimal state of the frictional interface (prestress) that promotes large events, out of all the statistically feasible distributions is the primary focus of this study. Following the approach of (Farazmand & Sapsis, 2017), we use an approximation of the chaotic attractor of the system during the inter-event period; this approximation uses Proper Orthogonal Decomposition (POD) to reduce dimension and account for the feasibility constraint. Representing the optimal prestress in a low dimensional space is favorable for the purpose of earthquake forecasting, as the data to constrain the physical parameters and current states of the system are sparse for earthquake cycles. We use the proximity of the current slip rate of the system to the slip rates of optimal solutions to propose an effective forecast method of large events. Our results suggest that this framework can be used to predict events in both space and time when we have access to the slip rate on the fault with certain resolution.

As our case study, we use a quasi-dynamic model with the standard rate-and-state friction with the aging law (Ruina, 1983). We apply this methodology to a 2D fault within a 3D medium, using a model setup analog to a model that has been shown to produce a realistic sequence of SSEs similar to those observed in Cascadia (Dal Zilio et al., 2020). We limit the analysis to the case of SSEs as in that case a quasi-dynamic approximation is justified which speeds up the numerical simulations (Rice, 1993; Thomas et al., 2014). We benefit from the fact that SSEs have a much larger ratio of nucleation size to the size of the fault compared to regular earthquakes. The range of magnitude of events in our 1000 years of synthetic data is 5.6-7.4 whereas for a large fault system with typical earthquakes, the range is much bigger. In other words, regular earthquake is a multi-scale process both in time and space, whereas, SSEs in our simulation are only multi-scale in time. Spatially small-scale processes in regular earthquakes contribute to more complexity of the system. This might limit the applicability of our method to these events without any further considerations.

2 MODEL SET UP

We use a quasi-dynamic model of slip events on a 2D fault in a 3D elastic medium, assuming rate-and-state friction with the aging law for the evolution of the state variable (θ):

$$\frac{\tau}{\bar{\sigma}_n} = \mu^* + a\ln(\frac{V}{V^*}) + b\ln(\frac{\theta V^*}{D_{RS}}), \tag{1a}$$

$$\frac{d\theta}{dt} = 1 - \frac{\theta V}{D_{RS}}. \tag{1b}$$

Here, $V((x,y),t) : \Gamma \times \mathbb{R}^+ \to \mathbb{R}^+$ is slip rate on the fault, $\theta((x,y),t) : \Gamma \times \mathbb{R}^+ \to \mathbb{R}^+$ is the state variable, $\tau((x,y),t) : \Gamma \times \mathbb{R}^+ \to \mathbb{R}^+$ is the frictional strength, $\bar{\sigma}_n$ is the effective normal stress, and a,b, D_{RS} are frictional properties of the surface (Γ) and are positive. μ^* and V^* are reference friction and slip rate respectively. The sign of $a-b$ determines the frictional regime of the fault. For $a-b>0$, the fault is Velocity Strengthening (VS); a jump in the velocity would increase the fault strength. Regions with $a-b>0$ suppress the rupture nucleation and acceleration. For $a-b<0$ fault is Velocity Weakening (VW); a jump in the slip rate (V), decreases the strength, and the fault is capable of nucleating earthquakes and accelerating the ruptures. $a-b$ varies spatially and is plotted in Fig 1(a).

The stress rate on the fault can also be written as:

$$\dot{\tau} = \mathcal{L}(V - V_{pl}) - \frac{G}{2c_s}\dot{V}, \tag{2}$$

where $\mathcal{L}$ is a pseudo-differential operator, and contains elastostatic response (Geubelle & Rice, 1995). Function $V_{pl}(x,y)$ is the plate slip rate which is assumed to be constant in time in this work. G and c_s are shear modulus and shear wave speed respectively. By taking the time derivative of Eq (1a), and eliminating $\dot{\tau}$ using Eq (2), we have a dynamical system for $u = [V, \theta]^\top$.

In practice, we consider a planar thrust fault with 90^o dip angle in elastic half-space that consists of a Velocity-Weakening (VW) patch (dotted area in Fig 1 (a)), within which ruptures can nucleate and propagate, surrounded by a Velocity-Strengthening (VS) patch where the propagation of seismic ruptures is inhibited (Fig 1 (a)). The fault is loaded by a surrounding fault that slips at a constant rate.

The model, with the properly selected and piece-wise constant parameters and initial conditions, exhibits a complex sequence of events with a variety of magnitudes distributed with a heavy tail consistent with the Gutenberg-Richter law (Fig 1 (b)). The shear stress on the locked portion of the fault (Fig 1 (c)) increases during the interevent period, leading to elastic strain energy build-up. During episodic slip events, the shear stress drops, and elastic strain energy is released and dissipated by frictional sliding and the radiation damping (Fig 1 (c)). To justify the assumption of ignoring wave propagation effects along the fault, we choose a parameter regime that produces SSEs in which V is small enough that the wave effects across the faults are negligible. The model parameters are taken from (Dal Zilio et al., 2020) to simulate SSEs similar to those in Cascadia.

For simplicity we did not include the effect of pore-pressure dilatancy. The frictional and physical properties of our problem are summarized in Table 1 and Fig 1.

The time series of the sequence of partial rupture with rare large ruptures is plotted in Fig 1 (c,d). Since stress is a function of θ and V in the rate-and-state friction, and θ is not measurable, we do not have access to stress distribution directly. As a result, in this work, we only assume that we have observations of the current slip rate when performing extreme event forecasting. In reality, the current slip rate on the fault can be indirectly constrained by measurements of ground surface displacements which involves an inversion that greatly reduces the spatial resolution of slip rate. Hence, we will also examine a simplified noisy scenario of slip rate measurement and study the performance of our algorithm with such condition. The slip potency deficit, which is the difference between the slip potency (integral of slip on the fault) and the slip potency if the fault was uniformly slipping at the loading rate, is plotted to show the chaotic behavior of the system and the rare occurrence of large events. The potency deficit builds up during the interevent period and drops during the episodic slip events (Fig 1 (e)). The time series of the magnitude of events is also plotted in Fig 1 (f). The maximum slip rate on the fault is plotted in Fig 2 with the dashed line as the threshold that we use for defining an event.

3 EXTREME EVENTS FORECASTING METHODS

3.1 Extreme events formulation

The dynamical system that comes from combining Eq 1 and 2 describes the coupled evolution of two functions $V((x,y),t) : \Gamma\times\mathbb{R}^+ \to \mathbb{R}^+$ and $\theta((x,y),t) : \Gamma\times\mathbb{R}^+ \to \mathbb{R}^+$. We assume $u = [V,\theta]^\top$ belongs to an appropriately chosen function space $\mathcal{U} : (\Gamma \times \mathbb{R}^+) \times (\Gamma \times \mathbb{R}^+) \to \mathbb{R}^+ \times \mathbb{R}^+$ and characterizes the state of the frictional interface at any given time and position on the fault. In the context of rate-and-state friction, shear stress is a function of the combination of variables (V,θ). Also, the evolution of the system is better rendered in the $\log_{10} u$ space. Consequently, we use the term 'prestress' to refer to the spatial distribution of $w = [\log_{10} V, \log_{10}\theta]^\top$ before a rupture; nonetheless, we formulate the dynamical model in terms of $u = (V,\theta)$.

The dynamical system for u is both multi-scale and chaotic and produces ruptures with a variety of sizes. The governing equation is

$$\frac{\partial u}{\partial t} = \mathcal{N}(u) \tag{3a}$$

$$u(x, y, 0) = u_0(x, y), \quad \forall (x, y) \in \Gamma \tag{3b}$$

where $\mathcal{N}$ is a nonlinear differential operator† that encompasses the quasi-dynamic approximation of the elastodynamics and the friction law (Eqs 1 and 2). We denote S^t as the solution operator for the dynamical system, mapping the current state forward by t time-units:

$$u(x, y, t) = S^t\left(u(x, y, 0)\right); \tag{4}$$

we can break this map into the components S^t_V and S^t_θ:

$$S^t\left(u(x, y, 0)\right) = \left[S^t_V\left(u(x, y, 0)\right), S^t_\theta\left(u(x, y, 0)\right)\right]^\top \tag{5}$$

We assume that the dynamical system has a global attractor $\mathcal{A}$ on which the dynamics are chaotic; we refer to this as the chaotic attractor in what follows.

Inspired by (Farazmand & Sapsis, 2019), we define event set $E(V_{\text{thresh}})$ for a prescribed threshold $V_{\text{thresh}} \in \mathbb{R}^+$ as:

$$E(V_{\text{thresh}}) = \{u \in \mathcal{U} : \sup_{(x,y)\in\Gamma} V(x, y) \geq V_{\text{thresh}}\} \tag{6}$$

By setting a proper event threshold (V_{thresh}), the event set includes both partial and full ruptures.

We now seek to determine the optimal feasible distributions of $\log_{10} u$ (prestress) in the interevent period that for a prediction horizon T lead to large magnitude events. By a 'feasible' prestress, we mean a prestress that is inside the chaotic attractor of the system; a combination of V and θ that is likely to be realized during the evolution of the dynamical system. We also want our criteria for optimality of prestress to be low-dimensional so that it can be captured using observations that are typically sparse in reality. We then use our low-dimensional critical prestress and only the current measurable state of the system (slip rate, which can in principle be estimated

† Technically a pseudo-differential operator

from geodetic measurements) to forecast the time and location of a possible large event in a time window horizon.

To formulate the question in mathematical terms, we introduce the moment magnitude of fault slip cumulated over the duration of integration Δt.

$$\widetilde{M}(u(x,y,t);\Delta t) = \frac{2}{3}\log_{10}\left(G\int_0^{\Delta t}\int_\Gamma S_V^{t'}(u(x,y,t))dx\,dy\;dt'\right) - 6. \tag{7}$$

where G is the elastic shear modulus. $\widetilde{M}$ measures the seismic moment on the fault in the $\log_{10}$ scale during Δt time-units (Scholz, 1989). $\widetilde{M}$ is slightly different from the definition of the moment magnitude (M) for one event because in $\widetilde{M}$, we take Δt to be a constant rather than being the actual duration of a particular event. In practice, we set it to be larger than the longest duration of events in our model. While we make use of $\widetilde{M}$ in our problem setup and benefit from its continuity over u, we will report the performance of the forecast of extreme events with a regular definition of moment magnitude (M).

We next define a cost function:

$$F(u;\Delta t,T) = \sup_{t\in[0,T)} \widetilde{M}(S^t(u);\Delta t) \tag{8}$$

where function $F:\mathcal{U}\to\mathbb{R}$ takes u as input and, for a prescribed prediction horizon (T) and event duration (Δt), finds the largest moment magnitude generated by the initial condition u. The optimal (most dangerous) feasible prestress conditions are determined by finding the local maxima (U^*) of $F(u;\Delta t,T)$ over $u\in\mathcal{A}\setminus E(V_{\text{thresh}})$ through an optimization process:

$$U^* = \{u^*|u^*\in\mathcal{A}\setminus E(V_{\text{thresh}}),\ u^* \text{ is a local maximizer of } F(u;\Delta t,T), F(u^*;\Delta t,T) > F_e^*\} \tag{9}$$

where F_e^* is some threshold for the magnitude to define a 'large' event. Eq (9) encompasses the main question of this work; that is finding optimal and statistically feasible prestress on the fault during the interevent period that makes large events in a short time window. In Eq (9), $u^*\in\mathcal{A}\setminus E(V_{\text{thresh}})$ ensures that u^* is inside the chaotic attractor (statistical feasibility constraint) and also in the interevent period; any state (u^*) outside $\mathcal{A}$ is inaccessible during the system's evolution because of the self-organization. After solving the optimization problem (Eq (9)), we use the 'similarity' of the current states of the system to solutions of Eq (9), as an indicator of an upcoming large event. We use the current slip rate as our only knowledge of the current state of the system as θ is not measurable. Solutions to Eq (9) are instability regions inside the chaotic attractor that generate large ruptures within the time span of $[0, T]$.

Set $\mathcal{A} \setminus E(V_{\text{thresh}})$ is a complicated set in the high-dimensional function space $\mathcal{U}$. Even if we can solve this optimization problem in this large space, it would be impractical to represent prestress in this high-dimensional space because the sparse data generally available in reality can only yield a low-dimensional model of the slip rate distribution on a fault. As a result, we approximate this set with a simpler set, characterized in a low-dimensional space using the POD method. This approach is developed in the next part.

3.2 Model reduction and forecast scheme

Many high-dimensional chaotic dynamical systems can be approximated by a low-dimensional system (Taira et al., 2017; Rowley & Dawson, 2017; Li et al., 2023; Brandstäter et al., 1983). Although the underlying dynamics of earthquakes and Slow Slip cycles are often chaotic (Huang & Turcotte, 1990; Becker, 2000; Anghel et al., 2004; Kato, 2016; Barbot, 2019), in certain examples, it has been observed that the chaotic attractors are low dimensional (Gualandi et al., 2020,0) which mathematically implies that we can approximate the evolution of the sequence of events using parameters in a finite-dimensional space instead of an infinite-dimensional function space. We use this property to reduce the dimensionality and approximate the chaotic attractor during the interevent period.

We approximate and reduce the dimensionality of the chaotic attractor of the system during the inter-event period using the POD technique (explained in Appendix A). The POD approach is widely adopted in the study of turbulent fluid flow (Taira et al., 2017); it is a linear model reduction method that uses singular value decomposition on a dataset of snapshot time series of the field, with the time-average removed. This process identifies spatial modes that are ranked according to their statistical significance in the dataset. Since the evolution of the system is better realized in the $w = \log_{10} u$ space, we apply the POD on the w rather than u. We denote by $\bar{w}$ the time average of the field (w) during the interevent period. POD technique inputs snapshots of $w - \bar{w}$

during the interevent period and gives orthonormal basis functions $\phi_i : \Gamma \times \Gamma \to \mathbb{R} \times \mathbb{R}$ and their associated variance λ_i for $i \geq 1$ where $\lambda_1 > \lambda_2 > ...$ which quantifies the statistical importance of each mode in the dataset. The subtraction of the mean is crucial because it ensures that the covariance matrix in the POD algorithm accurately reflects the variability and relationships within the dataset, rather than being influenced by the absolute positions of the data points. Then we can describe w, and consequently u, using a new coordinate system with the basis functions defined by ϕ_i's. Since the basis functions are ordered by the variance they capture in the data, the truncation and approximation of the field $w - \bar{w}$, with the first N_m POD modes captures a maximal statistical relevance (in the variance sense) of data between all possible N_m dimensional linear subspaces of $\log_{10} \mathcal{U}$.

We approximate $w : w \in \log_{10}(\mathcal{A} \setminus E(V_{\text{thresh}}))$ as perturbations around the time-average of w during the interevent period ($\bar{w} = [\bar{w}^V, \bar{w}^\theta]$) along those basis functions. Since we want to approximate only the interevent period we should exclude the event period ($E(V_{\text{thresh}})$) from the dataset of snapshots that are used to find POD modes (ϕ_i's). Following Blonigan et al. (2019), we constrain the perturbations along those eigenvectors to lie within a hyperellipse with a radius along each eigenvector proportional to the standard deviation of the data captured by each mode. In other words, we allow more perturbation along those directions that capture more statistical relevance in the data. The approximation of the chaotic attractor during the interevent period can be written as:

$$\log_{10}(\mathcal{A} \setminus E(V_{\text{thresh}})) \approx \Big\{ \bar{w} + \sum_{i=1}^{N_m} a_i \phi_i \Big| \sum_{i=1}^{N_m} \frac{a_i^2}{\lambda_i} \leq r_0^2 \Big\}. \tag{10}$$

where ϕ_i's ($i \geq 1$) are the orthonormal basis functions ordered by the data variance they capture (λ_i) in the centered dataset of time snapshots of $w - \bar{w}$ excluding the event period $E(V_{\text{thresh}})$. Here a_i is the amplitude of perturbation along ϕ_i and N_m is the number of basis functions we keep in our model reduction. The maximum perturbation along each basis function (ϕ_i) is constrained by the corresponding variance λ_i. One can play with the amplitude of the allowed perturbation which is represented by r_0.

Then Eq (9), which is an optimization problem in a high-dimensional function space $\mathcal{U}$, constrained on a complicated set $\mathcal{A} \setminus E(V_{\text{thresh}})$, can be approximated as an optimization problem in a low-dimensional ($\mathbb{R}^{N_m}$) space constrained within a hyperellipse. To solve the constrained optimization problem, we use optimal sampling in the framework of Bayesian optimization as it is useful when the objective function is costly to evaluate (Blanchard & Sapsis, 2021). The optimization method is described in Appendix B. During the optimization process, we collect all optimal prestresses ($w^* = [(\log V)^*, (\log\theta)^*]^\top$) in a set W^* that satisfies the feasibility constraint ($w^* \in \log_{10}(\mathcal{A} \setminus E(V_{\text{thresh}}))$) and has the value of $F(10^{w^*}; \Delta t, T)$ above the threshold F_e^*:

$$W^* := \left\{ w^* = \bar{w} + \sum_{i=1}^{N_m} a_i \phi_i \middle| \sum_{i=1}^{N_m} \frac{a_i^2}{\lambda_i} \leq r_0^2, F(10^{w^*}; \Delta t, T) > F_e^* \right\}. \tag{11}$$

W^* corresponds to the set of all of the prestresses leading to extreme events. To perform the spatial forecast, we need to record the evolution of each w^* for up to time T.

We use the proximity of the current state of the system to optimal states as an indicator of an upcoming large event. The current state of the system (w) is not measurable because θ is not measurable. Slip rate is the measurable component in w and we use it as a proxy of the current state of the system. Then, following Blonigan et al. (2019), we use the maximum cosine similarity between the $\log_{10}$ of the current slip rate ($\log V(t)$) and all of the optimal slip rates ($\log V_i^*$'s) in the set W^* as an indicator that signals an upcoming large event.

$$I(t) = \max_i \frac{\left\langle \log V(t) - \bar{w}^V, \log V_i^* - \bar{w}^V \right\rangle_{L^2}}{\| \log V(t) - \bar{w}^V \|_2 \| \log V_i^* - \bar{w}^V \|_2} \tag{12}$$

where $\langle \cdot, \cdot \rangle_{L^2}$ is the L^2 inner product, $\bar{w}^V$ is the average slip rate during interevent periods in the dataset, $\log V_i^*$ is the velocity component of the i^{th} optimal prestress (w_i^*), and $\| \ . \ \|_2$ is the L^2 norm. Note that $I(t)$ is only a function of the current slip rate on the fault.

4 RESULTS

4.1 Extreme event forecast

We use a simulation run for a total duration of 2200 years. We exclude the initial 200 years to eliminate the transient behavior, letting the system converge to its chaotic attractor. To define the event set (Eq (6)), we set the event threshold $V_{\text{thresh}} = 5 \times 10^{-8}(m/s)$. The event threshold is chosen such that we get reasonable scaling properties and also, we don't lose many events. The time series of the maximum slip velocity on the fault is plotted in Fig 2 in which V_{thresh} is denoted by a dashed line. We use data from $t = 200$ to $t = 1200$ years to perform the model reduction and find basis functions ϕ_i's and their corresponding variances λ_i's. We approximate $\mathcal{A} \setminus E(V_{\text{thresh}})$ using Eq (10) with a number of modes $N_m = 13$ which capture more than 85% variance of the data (based on the discussion in Appendix A). The mean of the field ($\bar{w} = [\bar{w}^V, \bar{w}^\theta]^\top$) together with the first four eigenfunctions $\phi_i = [\phi_i^V, \phi_i^\theta]^\top$ for interevent periods for the time range $t \in [200, 1200]$ (year) are plotted in Fig (3) with $\bar{w}$ as the empirical mean of the interevent states of the system w, ϕ_i^V as the i^{th} eigenfunction of the $\log_{10} V$ and ϕ_i^θ as the i^{th} eigenfunction of the $\log_{10} \theta$. Using ϕ_i's and λ_i's, we solve the optimization problem which has T (prediction horizon), Δt (event duration), and r_0 (amount of perturbation around $\bar{w}$) as hyper-parameters. We set the prediction horizon to $T = 0.5(year)$ and $\Delta t = 0.25(year)$ as the maximum duration of events in the time window of $t \in [200, 1200]$ year. With the increase of T, because of the effect of chaos, the predictability decreases and we would expect the performance of the algorithm to decrease.

The value of r_0 in the Eq (10) controls the size of the hyperellipse which is the constraint of the optimization problem. We perform the optimization for different values of r_0 (in Appendix B). For perturbations constrained within a small hyperellipse (small r_0), the algorithm does not find any optimal prestress that leads to a large event. This makes sense because, for small r_0, w is close to the $\bar{w}$ which is the average state of w during interevent periods. For very large r_0, the approximation of $\mathcal{A} \setminus E(V_{\text{thresh}})$ with a hyperellipse is less valid because we let the perturbation have amplitudes much larger than the standard deviation of each component along each eigenfunction. So, one should find an intermediate r_0 whose values of the cost function at the local maxima are larger but close to the maximum magnitude observed in the dataset. Here, we report results for $r_0 = 3$ which means that we don't let the prestress go outside the total 3 standard deviation range from $\bar{w}$ in $\mathbb{R}^{N_m}$. Unlike Blonigan et al. (2019) that, for a fluid flow problem, found a unique solution for their similar optimization problem, we see convergence to multiple local maxima ($w^* = [(\log V)^*, (\log \theta)^*]^\top$) for different algorithm initiations. As a result, to make our algorithm robust, we solve the optimization problem multiple times with random initiations.

The average prestress during the interevent period for the VW patch, and the prestress corresponding to one of the optimal solutions is plotted in Fig 4 (a,b). We have also plotted the dimensionless quantity $log_{10}(V\theta/D_{RS})$ in Fig 4 (c). The cumulative slip distribution corresponding to the event with magnitude 7.5 led by the optimal prestress is plotted in Fig 4 (d). We have plotted the slip rate (V), and the state variable (θ) corresponding to this particular optimal solution, together with the convergence of the optimization algorithm, in Appendix B. We record the rupture extent of optimal solutions (a total of 12 local maxima) that have $F_e^* > 7.4$ to use for spatial prediction. These optimal prestress distributions are relatively complex with heterogeneities both along the strike and along the dip directions. Because we have only approximated the chaotic attractor by a hyperellipse, the solutions of the optimization problem are unlikely to be exactly observed in the simulation of the dynamical system evolution. However, because the non-linear dynamical system can be linearized locally, it can be assumed that if the system gets close to any of these optimal solutions, due to stress redistributions by events of all sizes, a slip event should follow with a head time (the difference between the current time and the time of occurrence of the large slip event) and a slip distribution close to this optimal solution. We rely on this principle to forecast the time and location of large slip events. It is interesting to note that with the defined event threshold, we don't see any full-system size rupture in the forward simulation. However, if we start from homogeneous initial conditions, we see periodic fault-size ruptures. This solution is probably unstable or stable with a small basin of attraction because a relatively small perturbation from the homogeneous initial condition leads to the convergence of the system to its chaotic attractor.

The indicator $I(t)$ (Eq (12)), can effectively forecast large events for the dataset from $t = 1200$ to $t = 2200$ years with a prediction horizon of $T = 0.5$ (year). To illustrate, $I(t)$ is plotted alongside F in Fig 5 (a). A high value of F shows an upcoming large event in the time interval $[0, T]$ and we observe that when F rises, the indicator signals a large event by rising to large values. We define a threshold I_e above which we signal an upcoming large event. We also define F_e as the threshold for extreme events; whenever F is larger than F_e we say that an extreme event is going to happen in the next T year(s). The values of F_e and I_e are determined such that the proportion of the true positive and true negative forecasts of extreme events are maximized. By recording the values of $I(t)$ and $F(t)$, we can empirically find the conditional probability $P(F|I)$ (Fig 5 (b)). Values of F_e and I_e are denoted by the white vertical and horizontal dashed lines in Fig 5 (b). The probability in this context is with respect to the invariant measure of the chaotic attractor. Different quadrants of this plot show four conditions including true negative, false negative, true positive, and false positive from bottom left counterclockwise to top left. While most of the high values of $P(F|I)$ lie inside the true negative and true positive regions, it is essential to acknowledge that the probabilities of false negative and false positive are not zero. We also plot the empirical probability of observing an event greater than F_e given the knowledge of I, ($P[F > F_e|I]$). This value which is denoted by P_{ee} is plotted in Fig 5 (c). P_{ee} consistently rises to values close to one, which is another way to show that the indicator I can be used as a predictor of large events. We plot the forecast of rupture extent in Fig 5 (d) which shows the effectiveness of both spatial and temporal forecasts of large events. Since we have recorded the rupture extent of optimal solutions (elements in set W^*), as soon as the current state of the system gets close to the i^{th} optimal solution and the indicator signals an upcoming event ($I(t) > I_e$), we propose the recorded rupture extent of the i^{th}optimal solution as the spatial forecast. Fig 5 (e) shows the temporal forecast of events with the magnitude of events plotted in blue. Whenever the indicator has a value greater than I_e, we forecast (red region) that an event larger than $F_e = 6.9$ (black dashed line) will happen. Red shows the temporal prediction of events larger than F_e. The magnitude in Fig 5 (e) is calculated according to the regular definition of the magnitude of an event (i.e. by integrating the slip velocity above the threshold over the exact duration of the event). In Supplemental Video 1, an animation of this prediction is available.

4.2 Forecast with Partial Observation of Slip Rate

So far, we have assumed that we have full access to the slip rate on the fault. Here, we relax this assumption and use slip rate measurements only at a few points on the fault (diamonds in Fig 1 (a)). We denote $\hat{V} : \mathbb{R}^{N_p} \times \mathbb{R}^+ \to \mathbb{R}^+$ as the time series of partial slip rate observation, where N_p is the number of points of slip rate measurements and we take it to be 16 in this case study.

We assume that these points are at the center of the fault along the depth and have equal distances along the strike. We redefine the indicator $I(t)$ for this special case as follows:

$$I(t) = \max_i \frac{\left\langle \log \hat{V}(t) - \hat{\bar{w}}^V, \log \hat{V}_i^* - \hat{\bar{w}}^V \right\rangle_{\mathbb{R}^{N_p}}}{\| \log \hat{V}(t) - \hat{\bar{w}}^V \|_2 \| \log \hat{V}_i^* - \hat{\bar{w}}^V \|_2} \tag{13}$$

where $\hat{V}_i^*$ is the slip rate at the measurement points (diamonds in Fig 1 (a)) of the i^{th} optimal solution in the set W^*. $\hat{\bar{w}}^V$ is the average slip rate at the measurement points during the interevent period. $\langle , \rangle_{\mathbb{R}^{N_p}}$ is the inner product in $\mathbb{R}^{N_p}$. Fig 6 shows the forecast performance in the limited slip rate measurement scenario. The general consistent increase in $I(.)$ when the function $F(.)$ rises is visible in Fig 6 (a). Fig 6 (b) and (c) show statistically the performance of the predictor. While most of the probability mass of $P(F|I)$ belongs to true positive and true negative we should appreciate that there is more probability mass in the false positive quadrant compared to the scenario in which we have full access to the slip rate. This can be observed better in Fig 6 (c), (d), and (e). Although as I increases, P_{ee} increases consistently, P_{ee} is almost 0.9 when I is the maximum which suggests that there is a 10% chance of a false positive signal when I takes its maximum value. This false positive can also be observed in Fig 6 (d) and (e) around the year 1610. While is it important to appreciate the limitations, the overall performance is satisfying. To reduce this limitation, one can use filtering methods to invert and approximate slip rates at a few more points on the fault to improve the performance.

4.3 Impact of Low-Pass Filter Noise on Prediction Accuracy

In this part, we illustrate a limitation of our method as we lose more and more information with noisier data. Real-world slip inversion on the fault has inherent low-pass filter noise because the process of finding slip on the fault from surface displacements involves filtering techniques that inevitably introduce this type of noise. These techniques are necessary due to the measurement limitations, which cannot capture high-frequency variations accurately, leading to a smoother and potentially less precise representation of the actual slip rates. We apply a Gaussian kernel to the synthetic slip rate data, mimicking the characteristics of realistic datasets. This approach allows us to systematically assess the impact of noise on the performance of extreme event prediction. By varying the standard deviation of the Gaussian kernel, we evaluate how different noise levels affect the algorithm's accuracy. The standard deviation is expressed in a dimensionless form relative to the width of the width of the VW zone.

We assume that the slip rate is corrupted by a Gaussian kernel which is defined mathematically as:

$$G(x,y) = \frac{1}{2\pi\sigma^2} \exp\left(-\frac{x^2+y^2}{2\sigma^2}\right). \tag{14}$$

where σ is the standard deviation of the Gaussian kernel, controlling the extent of the smoothing effect. By convolving this kernel with the original slip rate data $V(x,y)$, we obtain the noisy slip rate $V'(x,y)$:

$$V'(x,y) = \int_\Gamma V(x',y') \cdot G(x-x', y-y')\, dx'\, dy' \tag{15}$$

To visually demonstrate the effect of the kernel on the data, we plotted one snapshot of slip rate without noise in Fig 7 (a) and then applied the low-pass filter with different standard deviation on that snapshot of the velocity and plot them in Fig 7 (b,c,d). The conditional probability $P(F|I)$ for a 1000 year long data that are corrupted by these noise levels are plotted in Fig 7 (e,f,g). As the noise level increases the probability mass in the upper left (false positive) and lower right (false negative) increases. Fig 7 (f) and (g) show that with a standard deviation greater than $0.5W_{VW}$, we have a large probability of a false signal. This is a limitation of our work and potentially considering more POD modes, using data assimilation techniques to more accurately invert for slip on the fault, and considering the history of the time series are some of the methods that can be used to improve the performance when the noise level is large.

5 DISCUSSION

Our results demonstrate the possibility of predicting the time, size, and spatial extent of extreme events in a simplified dynamical model of earthquake sequences based on the instantaneous observation of fault slip rate. By constraining the prestress on a fault to the only feasible ones and solving an optimization problem, we found the optimal prestress in a low dimensional space. Optimal prestress refers to configurations of stress heterogeneity on the fault triggering large events within small time windows. Identifying the optimal prestress distributions that are also statistically accessible during the earthquake cycle is pivotal.

Prestress self-organizes into a chaotic attractor which occupies only a small fraction of all possible stress distributions on the fault. The identification of the optimal prestress within this reduced set is crucial for two reasons. First, it helps establish a low-dimensional representation of optimal prestress; the significance of reduced-order proxy of critical prestress is even more important for earthquakes than SSEs, primarily due to the scarcity of observational data obtained from paleoseismic records. Second, everything outside this set remains unseen during the earthquake cycle's evolution. If that was not the case, the space of hypothetical stress distribution possibly leading to large events would be intractable.

In section 4.2, we studied a scenario in which the slip rate is known at only a few points on the fault. The results are almost as good as when we have full access to the slip rate on the fault because the slip evolution at neighboring points on the fault is strongly correlated due to elastic coupling. This result most likely benefits from large nucleation length for SSEs which is generally not true for earthquakes. The nucleation length for a 1D fault for mode III is given by $h_{ra} = \frac{2GD_{RS}b}{\pi\bar{\sigma}(b-a)^2}$ (Rubin & Ampuero, 2005), where G is shear modules, $\bar{\sigma}$ is the effective normal stress, and a, b, D_{RS} are frictional parameters.. For a 2D fault, the nucleation size is given by $h = (\pi^2/4)h_{ra}$ (Chen & Lapusta, 2009), and is $29.7(km)$ in our model, whereas the width of the VW zone is $W_{VW} = 25(km)$.

Slip rate data of a fault is determined through the inversion of surface displacement, which results in low spatial resolution. We therefore studied the performance of extreme event prediction when the synthetic slip rate is corrupted by a low pass filter. Our results Fig 7 indicate that predictability is compromised when the standard deviation of the low-pass filter kernel gets larger and larger. This finding highlights a limitation in the application of our study in its current form when this type of noise is prevalent in the data. Addressing this limitation will be a focus of our future work. Potential approaches include incorporating additional components into the extreme event criteria and solving a data assimilation problem, such as using the Ensemble Kalman filter, to more accurately invert for slip rates on the fault.

6 CONCLUSION

Our study suggests that the chaotic nature of earthquake sequences is not an insurmountable obstacle to time-dependent earthquake forecasting. However, we acknowledge that we considered a favorable model setup designed to produce SSEs. It would be now interesting to test this approach in the case of a model setup producing regular earthquakes (i.e., with slip rates of $1cm/s$ to $1m/s$ to be comparable to real earthquakes) with larger ratios of fault dimensions to nucleation size and with a larger range of earthquake magnitudes (Barbot, 2021; Cattania, 2019; Lambert & Lapusta, 2021). This is doable although computationally challenging. The amplitude of the stress heterogeneity would be more substantial for regular earthquakes, where dynamic wave-mediated stresses allow for rupture propagation over lower stress conditions than for aseismic slip, particularly in models with stronger dynamic weakening or with persistent heterogeneity such as normal stress perturbations. (Noda et al., 2009; Lambert et al., 2021) .

It is expected that earthquake sequences would then show more complexity due to the cascading effects which are responsible for foreshocks and aftershocks in natural earthquake sequences, and which are not present in our simulations. In that regard, Blonigan et al. (2019) reported that the performance of their prediction of rare events diminishes with the increase in Reynolds number in their turbulent flow case. It is possible that we have the same limitation as the ratio of the nucleation size to the dimensions of the fault decreases.

ACKNOWLEDGMENTS

The authors HK and J-PA express their sincere gratitude to the National Science Foundation (NSF) for their financial support of this research project, through the Industry-University Collaborative Research Center Geomechanics and Mitigation of Geohazards (award #1822214). Author AMS is grateful to DoD for support as a Vannevar Bush Faculty Fellow. Additionally, the authors are grateful for the valuable input and discussion provided by Nadia Lapusta, Brendan Meade, Themis Sapsis, Adriano Gualandi, Alba Rodriguez, Camilla Cattania, Elif Oral, Mateo Acosta, Kelian Dascher-Cousineau, Zachary R Ross, Jan Dirk Jansen, Kyungjae Im. The authors also extend their appreciation to Eric Dunham and the other anonymous reviewer for their constructive feedback and insightful comments.

Data Availability Statement

We used a model of a 2D thrust fault in a 3D medium governed by rate-and-state friction with aging law for the evolution of state variable (θ). The model parameters are summarized in Table 1. To simulate the forward model, we use the QDYN software[‡], which is an open-source code to simulate earthquake cycles (Luo et al., 2017). We use the POD technique to reduce the dimensionality of the problem. This method is reviewed in Appendix A. To solve the optimization problem we use the Bayesian optimization method (Brochu et al., 2010; Blanchard & Sapsis, 2021) that is reviewed in Appendix B. We used the open source code available on GitHub[§] for solving the optimization problem.

Supplementary Materials

Supplemental Videos: Movie S1 to Movie S2

‡ https://github.com/ydluo/qdyn

§ https://github.com/ablancha/gpsearch

References

Anghel, M., Ben-Zion, Y., & Rico-Martinez, R., 2004. Dynamical System Analysis and Forecasting of Deformation Produced by an Earthquake Fault, in *Computational Earthquake Science Part I*, Pageoph Topical Volumes, pp. 2023–2051, eds Donnellan, A., Mora, P., Matsu'ura, M., & Yin, X.-c., Birkhäuser, Basel.

Avouac, J.-P., 2015. From Geodetic Imaging of Seismic and Aseismic Fault Slip to Dynamic Modeling of the Seismic Cycle, *Annual Review of Earth and Planetary Sciences*, **43**(1), 233–271, _eprint: https://doi.org/10.1146/annurev-earth-060614-105302.

Barbot, S., 2019. Slow-slip, slow earthquakes, period-two cycles, full and partial ruptures, and deterministic chaos in a single asperity fault, *Tectonophysics*, **768**, 228171.

Barbot, S., 2021. A Spectral Boundary-Integral Method for Quasi-Dynamic Ruptures of Multiple Parallel Faults, *Bulletin of the Seismological Society of America*, **111**(3), 1614–1630.

Barbot, S., Lapusta, N., & Avouac, J.-P., 2012. Under the Hood of the Earthquake Machine: Toward Predictive Modeling of the Seismic Cycle, *Science*, **336**(6082), 707–710, Publisher: American Association for the Advancement of Science.

Becker, T. W., 2000. Deterministic Chaos in two State-Variable Friction Sliders and the Effect of Elastic Interactions, in *Geocomplexity and the Physics of Earthquakes*, pp. 5–26, American Geophysical Union (AGU), _eprint: https://onlinelibrary.wiley.com/doi/pdf/10.1029/GM120p0005.

Blanchard, A. & Sapsis, T., 2021. Bayesian optimization with output-weighted optimal sampling, *Journal of Computational Physics*, **425**, 109901.

Blonigan, P. J., Farazmand, M., & Sapsis, T. P., 2019. Are extreme dissipation events predictable in turbulent fluid flows?, *Physical Review Fluids*, **4**(4), 044606, Publisher: American Physical Society.

Brandstäter, A., Swift, J., Swinney, H. L., Wolf, A., Farmer, J. D., Jen, E., & Crutchfield, P. J., 1983. Low-Dimensional Chaos in a Hydrodynamic System, *Physical Review Letters*, **51**(16), 1442–1445, Publisher: American Physical Society.

Brochu, E., Cora, V. M., & de Freitas, N., 2010. A Tutorial on Bayesian Optimization of Expensive Cost Functions, with Application to Active User Modeling and Hierarchical Reinforcement

Learning, arXiv:1012.2599 [cs].

Cattania, C., 2019. Complex Earthquake Sequences On Simple Faults, *Geophysical Research Letters*, **46**(17-18), 10384–10393, _eprint: https://onlinelibrary.wiley.com/doi/pdf/10.1029/2019GL083628.

Chen, T. & Lapusta, N., 2009. Scaling of small repeating earthquakes explained by interaction of seismic and aseismic slip in a rate and state fault model, *Journal of Geophysical Research: Solid Earth*, **114**(B1), _eprint: https://onlinelibrary.wiley.com/doi/pdf/10.1029/2008JB005749.

Dal Zilio, L., Lapusta, N., & Avouac, J., 2020. Unraveling Scaling Properties of Slow-Slip Events, *Geophysical Research Letters*, **47**(10).

Farazmand, M. & Sapsis, T. P., 2017. A variational approach to probing extreme events in turbulent dynamical systems, *Science Advances*, **3**(9), e1701533, Publisher: American Association for the Advancement of Science.

Farazmand, M. & Sapsis, T. P., 2019. Extreme Events: Mechanisms and Prediction, *Applied Mechanics Reviews*, **71**(5).

Geubelle, P. H. & Rice, J. R., 1995. A spectral method for three-dimensional elastodynamic fracture problems, *Journal of the Mechanics and Physics of Solids*, **43**(11), 1791–1824.

Gualandi, A., Avouac, J.-P., Michel, S., & Faranda, D., 2020. The predictable chaos of slow earthquakes, *Science Advances*, **6**(27), eaaz5548, Publisher: American Association for the Advancement of Science.

Gualandi, A., Faranda, D., Marone, C., Cocco, M., & Mengaldo, G., 2023. Deterministic and stochastic chaos characterize laboratory earthquakes, *Earth and Planetary Science Letters*, **604**, 117995.

Gutenberg, B. & Richter, C. F., 1950. Seismicity of the Earth and associated phenomena, *MAUSAM*, **1**(2), 174–176, Number: 2.

Huang, J. & Turcotte, D. L., 1990. Are earthquakes an example of deterministic chaos?, *Geophysical Research Letters*, **17**(3), 223–226, _eprint: https://onlinelibrary.wiley.com/doi/pdf/10.1029/GL017i003p00223.

Kaneko, Y., Avouac, J.-P., & Lapusta, N., 2010. Towards inferring earthquake patterns from geodetic observations of interseismic coupling, *Nature Geoscience*, **3**(5), 363–369, Number: 5 Publisher: Nature Publishing Group.

Kato, N., 2016. Earthquake Cycles in a Model of Interacting Fault Patches: Complex Behavior at Transition from Seismic to Aseismic Slip, *Bulletin of the Seismological Society of America*, **106**(4), 1772–1787.

Konca, A. O., Avouac, J.-P., Sladen, A., Meltzner, A. J., Sieh, K., Fang, P., Li, Z., Galetzka, J., Genrich, J., Chlieh, M., Natawidjaja, D. H., Bock, Y., Fielding, E. J., Ji, C., & Helmberger, D. V., 2008. Partial rupture of a locked patch of the Sumatra megathrust during the 2007 earthquake sequence, *Nature*, **456**(7222), 631–635, Number: 7222 Publisher: Nature Publishing Group.

Lambert, V. & Lapusta, N., 2021. Resolving Simulated Sequences of Earthquakes and Fault Interactions: Implications for Physics-Based Seismic Hazard Assessment, *Journal of Geophysical Research: Solid Earth*, **126**(10), e2021JB022193, _eprint: https://onlinelibrary.wiley.com/doi/pdf/10.1029/2021JB022193.

Lambert, V., Lapusta, N., & Faulkner, D., 2021. Scale Dependence of Earthquake Rupture Prestress in Models With Enhanced Weakening: Implications for Event Statistics and Inferences of Fault Stress, *Journal of Geophysical Research: Solid Earth*, **126**(10), e2021JB021886, _eprint: https://onlinelibrary.wiley.com/doi/pdf/10.1029/2021JB021886.

Lapusta, N. & Liu, Y., 2009. Three-dimensional boundary integral modeling of spontaneous earthquake sequences and aseismic slip, *Journal of Geophysical Research: Solid Earth*, **114**(B9), _eprint: https://onlinelibrary.wiley.com/doi/pdf/10.1029/2008JB005934.

Lapusta, N. & Rice, J. R., 2003. Nucleation and early seismic propagation of small and large events in a crustal earthquake model, *Journal of Geophysical Research: Solid Earth*, **108**(B4), _eprint: https://onlinelibrary.wiley.com/doi/pdf/10.1029/2001JB000793.

Lapusta, N., Rice, J. R., Ben-Zion, Y., & Zheng, G., 2000. Elastodynamic analysis for slow tectonic loading with spontaneous rupture episodes on faults with rate- and state-dependent friction, *Journal of Geophysical Research: Solid Earth*, **105**(B10), 23765–23789, _eprint: https://onlinelibrary.wiley.com/doi/pdf/10.1029/2000JB900250.

Li, M., Jain, S., & Haller, G., 2023. Model reduction for constrained mechanical systems via spectral submanifolds, *Nonlinear Dynamics*, **111**(10), 8881–8911.

Luo, Y., Ampuero, J. P., Galvez, P., Ende, M. v. d., & Idini, B., 2017. QDYN: a Quasi-DYNamic earthquake simulator (v1.1).

Marone, C., 1998. Laboratory-Derived Friction Laws and Their Application to Seismic Faulting, *Annual Review of Earth and Planetary Sciences*, **26**(1), 643–696, _eprint: https://doi.org/10.1146/annurev.earth.26.1.643.

Marsan, D. & Tan, Y. J., 2020. Maximum Earthquake Size and Seismicity Rate from an ETAS Model with Slip Budget, *Bulletin of the Seismological Society of America*, **110**(2), 874–885.

Michel, S., Gualandi, A., & Avouac, J.-P., 2019. Similar scaling laws for earthquakes and Cascadia slow-slip events, *Nature*, **574**(7779), 522–526, Number: 7779 Publisher: Nature Publishing Group.

Murray, J. & Segall, P., 2002. Testing time-predictable earthquake recurrence by direct measurement of strain accumulation and release, *Nature*, **419**(6904), 287–291, Number: 6904 Publisher: Nature Publishing Group.

Noda, H., Dunham, E. M., & Rice, J. R., 2009. Earthquake ruptures with thermal weakening and the operation of major faults at low overall stress levels, *Journal of Geophysical Research: Solid Earth*, **114**(B7), _eprint: https://onlinelibrary.wiley.com/doi/pdf/10.1029/2008JB006143.

Okubo, P. G. & Aki, K., 1987. Fractal geometry in the San Andreas Fault System, *Journal of Geophysical Research: Solid Earth*, **92**(B1), 345–355, _eprint: https://onlinelibrary.wiley.com/doi/pdf/10.1029/JB092iB01p00345.

Reid, H., 1910. *The Mechanics of the Earthquake, The California Earthquake of April 18, 1906, Report of the State Investigation Commission*, vol. 2.

Rice, J. R., 1993. Spatio-temporal complexity of slip on a fault, *Journal of Geophysical Research: Solid Earth*, **98**(B6), 9885–9907, _eprint: https://onlinelibrary.wiley.com/doi/pdf/10.1029/93JB00191.

Rowley, C. W. & Dawson, S. T., 2017. Model Reduction for Flow Analysis and Control, *Annual Review of Fluid Mechanics*, **49**(1), 387–417, _eprint: https://doi.org/10.1146/annurev-fluid-010816-060042.

Rubin, A. M. & Ampuero, J.-P., 2005. Earthquake nucleation on (aging) rate and state faults, *Journal of Geophysical Research: Solid Earth*, **110**(B11), _eprint: https://onlinelibrary.wiley.com/doi/pdf/10.1029/2005JB003686.

Ruina, A., 1983. Slip instability and state variable friction laws, *Journal of Geophysical Research: Solid Earth*, **88**(B12), 10359–10370, _eprint: https://onlinelibrary.wiley.com/doi/pdf/10.1029/JB088iB12p10359.

Sagy, A., Brodsky, E. E., & Axen, G. J., 2007. Evolution of fault-surface roughness with slip, *Geology*, **35**(3), 283–286.

Scholz, C. H., 1989. *Mechanics of faulting*, Publication Title: Annual review of earth and planetary sciences. Vol. 17 ISSN: 0084-6597.

Shaw, B. E. & Rice, J. R., 2000. Existence of continuum complexity in the elastodynamics of repeated fault ruptures, *Journal of Geophysical Research: Solid Earth*, **105**(B10), 23791–23810, _eprint: https://onlinelibrary.wiley.com/doi/pdf/10.1029/2000JB900203.

Taira, K., Brunton, S. L., Dawson, S. T. M., Rowley, C. W., Colonius, T., McKeon, B. J., Schmidt, O. T., Gordeyev, S., Theofilis, V., & Ukeiley, L. S., 2017. Modal Analysis of Fluid Flows: An Overview, *AIAA Journal*, **55**(12), 4013–4041, Publisher: American Institute of Aeronautics and Astronautics.

Thomas, M. Y., Lapusta, N., Noda, H., & Avouac, J.-P., 2014. Quasi-dynamic versus fully dynamic simulations of earthquakes and aseismic slip with and without enhanced coseismic weakening, *Journal of Geophysical Research: Solid Earth*, **119**(3), 1986–2004, _eprint: https://onlinelibrary.wiley.com/doi/pdf/10.1002/2013JB010615.

Utsu, T., Ogata, Y., S, R., & Matsu'ura, 1995. The Centenary of the Omori Formula for a Decay Law of Aftershock Activity, *Journal of Physics of the Earth*, **43**(1), 1–33.

Table 1. Physical Properties

VW region	a	0.004
	b	0.014
VS region	a	0.019
	b	0.014
Characteristic slip weakening distance	D_{RS}	$0.045(m)$
Reference steady state slip rate	V^*	$10^{-6}\frac{m}{s}$
Reference steady-state friction coefficient	f^*	0.6
Effective normal stress	$\bar{\sigma}_n$	$10(MPa)$
Shear modulus	G	$30(GPa)$
Plate loading Velocity	V_{pl}	$40(mm/year)$

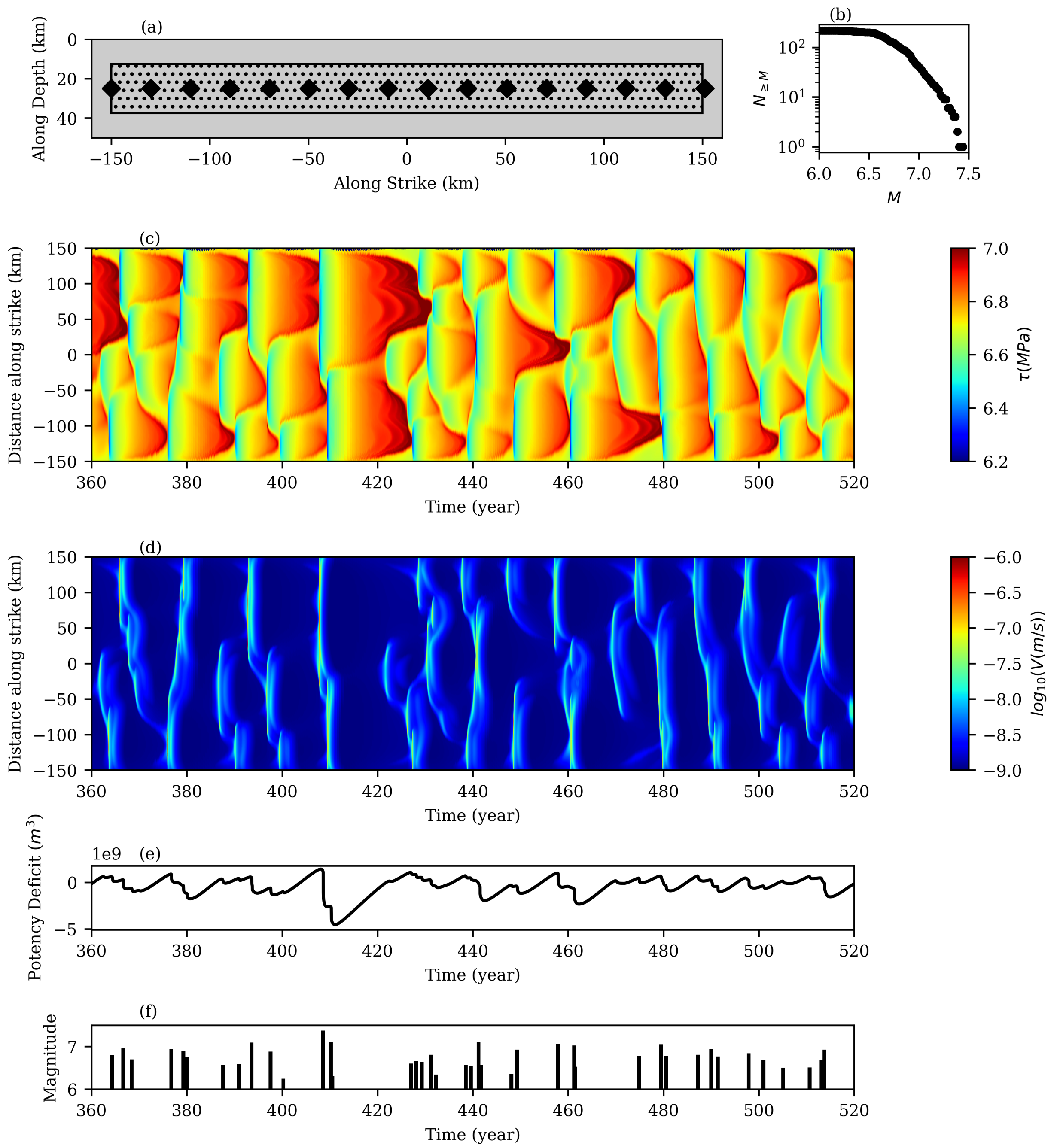

Figure 1. Geometry of the fault (a). The VW patch is the dotted area that is surrounded by the VS patch. The diamonds are the locations of slip rate measurements for the scenario in which we do not have full access to the slip rate on the entire fault. The number of events with a magnitude greater than M, (N_M) is plotted in (b) for 1000 years of simulation time. Maximum stress along the depth for the VW patch is plotted as a function of distance along strike and time (c). The maximum slip rate for the VW patch along the depth is plotted as a function of distance along strike and time (d). The time-series of the potency deficit and magnitudes are plotted in (e) and (f) respectively.

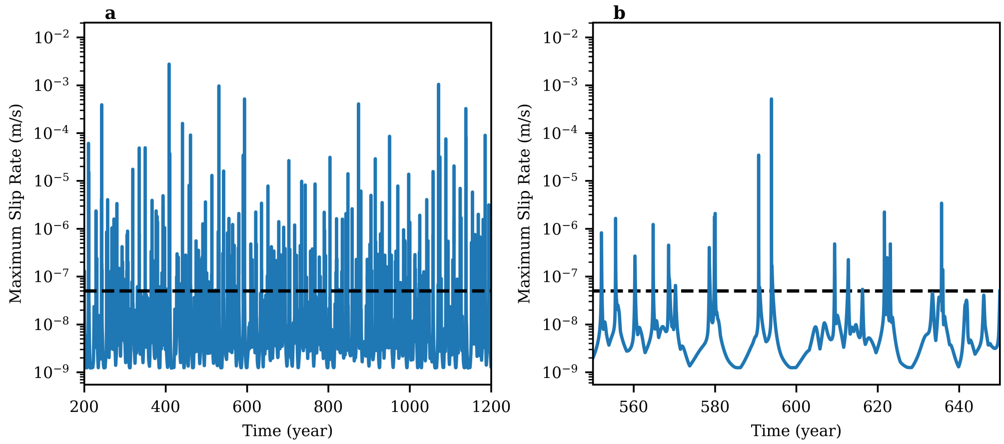

Figure 2. Time series of the maximum slip rate for a period of 1000 years (a) and 100 years (b) with threshold velocity denoted by a dashed line.

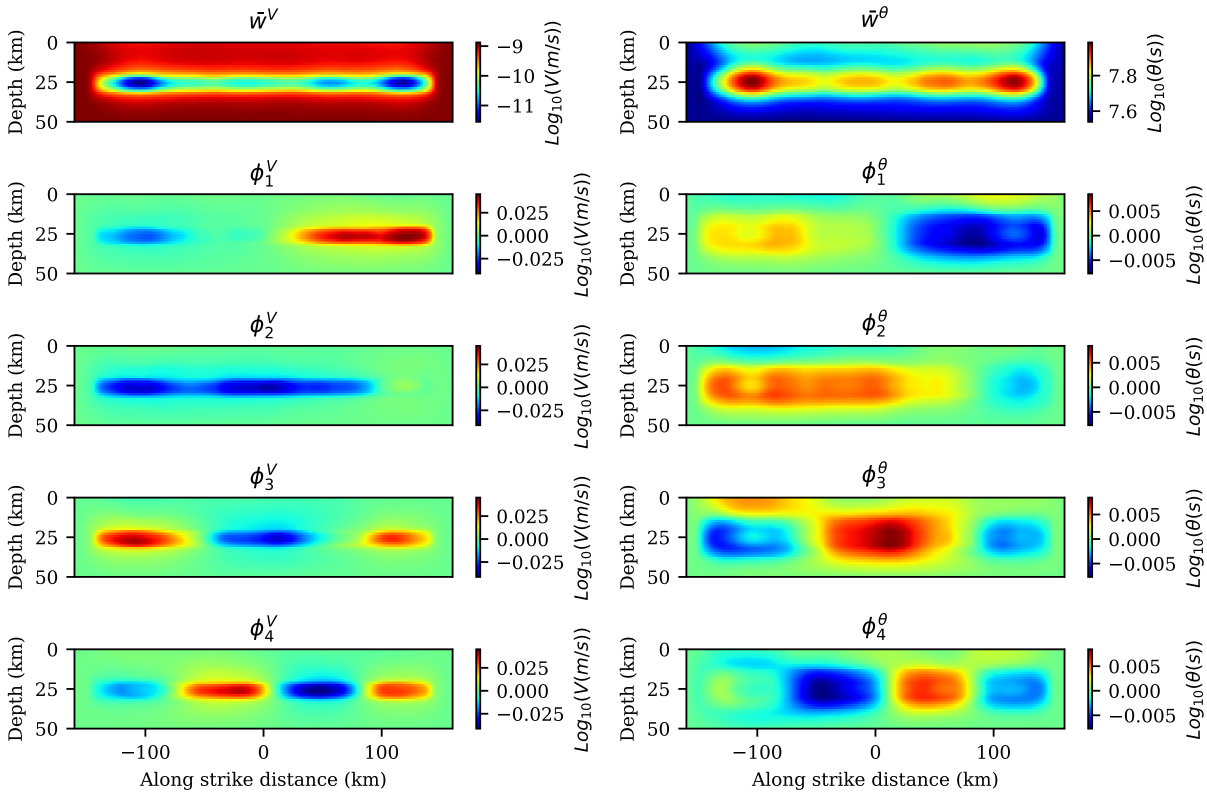

Figure 3. Average of the $\log_{10}$ of slip rate ($\bar{w}^V$) and state variable ($\bar{w}^\theta$) during the interevent periods, and first four eigenfunctions for $\log_{10}$ of slip rate (ϕ_i^V for $1 \le i \le 4$) and state variable (ϕ_i^θ for $1 \le i \le 4$) that are ordered by the variance they capture in the datasets. The dataset contains interevent snapshots of $\log_{10}$ of slip rate and state variable during the interevent periods from the year 200 to 1200.

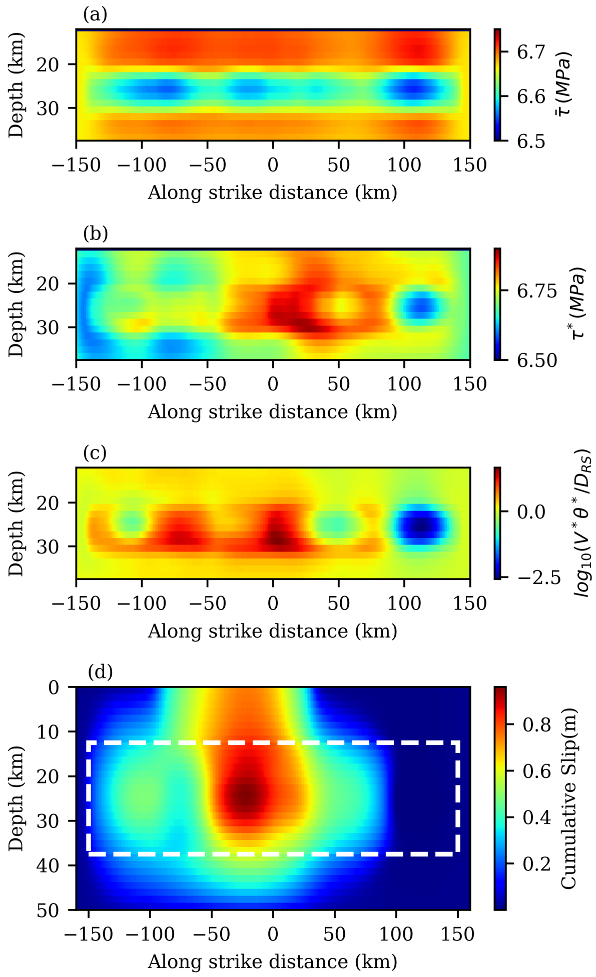

Figure 4. Average of the shear stress on the VW patch of the fault during the interevent period (a). One of the local optimal prestress distributions that leads to an event with a magnitude of 7.5 (b). The dimensionless quantity $log_{10}(V\theta/D_{RS})$ for the optimal prestress is plotted in (c). The corresponding cumulative slip of the event that happens right after starting from optimal prestress (d). To increase the readability (a,b,c) are plotted only for the VW patch. The VW patch in (d) is denoted by the dashed white line.

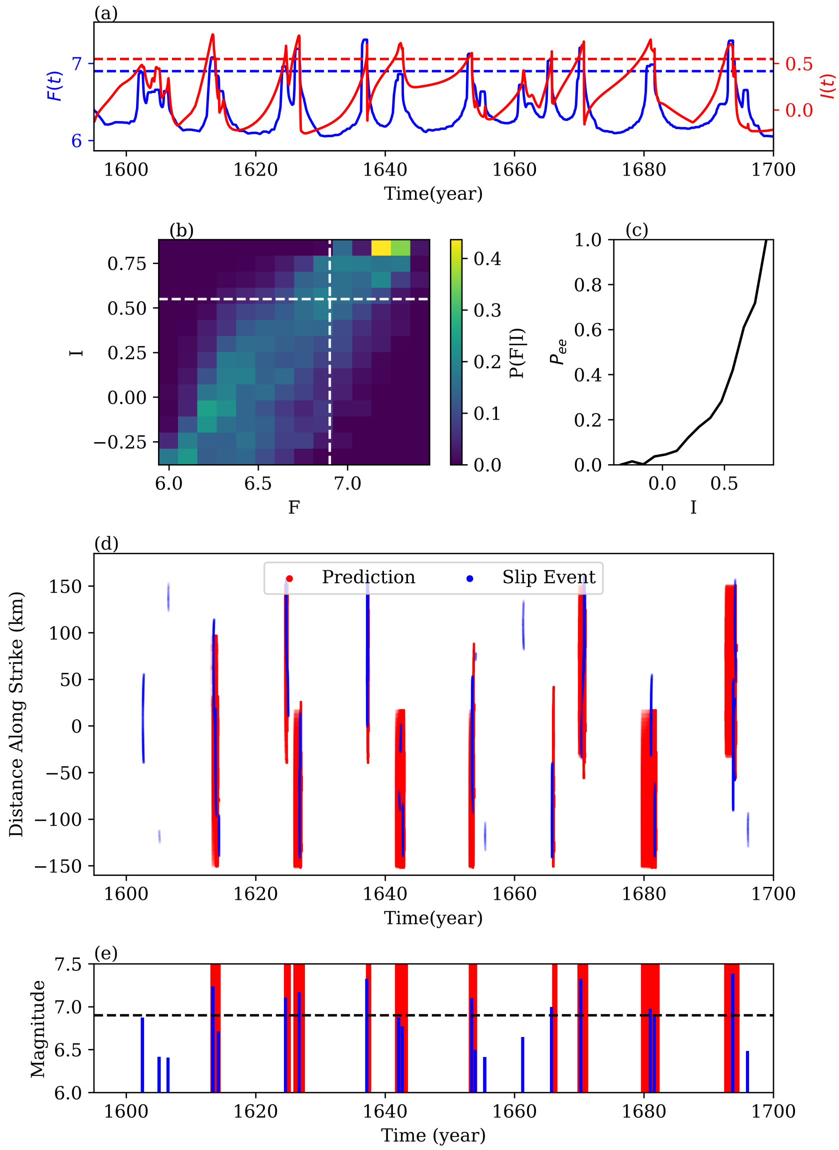

Figure 5. Spatiotemporal prediction of events. The time series of the functions F and I show that I rises when there is an upcoming large event (F is large), and it goes down when there is no upcoming large event. The blue and red dashed lines correspond to F_e and I_e (a). The empirical conditional probability $P(F|I)$. The vertical and horizontal dashed lines are F_e, and I_e respectively (b). The empirical probability of having an event with the value $\widetilde{M}$ greater than F_e in the next $0.5(year)$ as a function of the value of the indicator I (c). The spatiotemporal prediction of events is plotted by red where blue is the actual events in the dataset (d). Prediction of the magnitudes with the blue bars as the magnitude of events in the dataset. The horizontal axis for the blue bars denotes the time when an event starts. Red regions denote the times of high probability of large events (above magnitude 6.9 (dashed line)) based on our indicator (e). The statistical plots (b,c) are calculated based on 1000 years of data in the test set (data from the year 1200 to 2200)

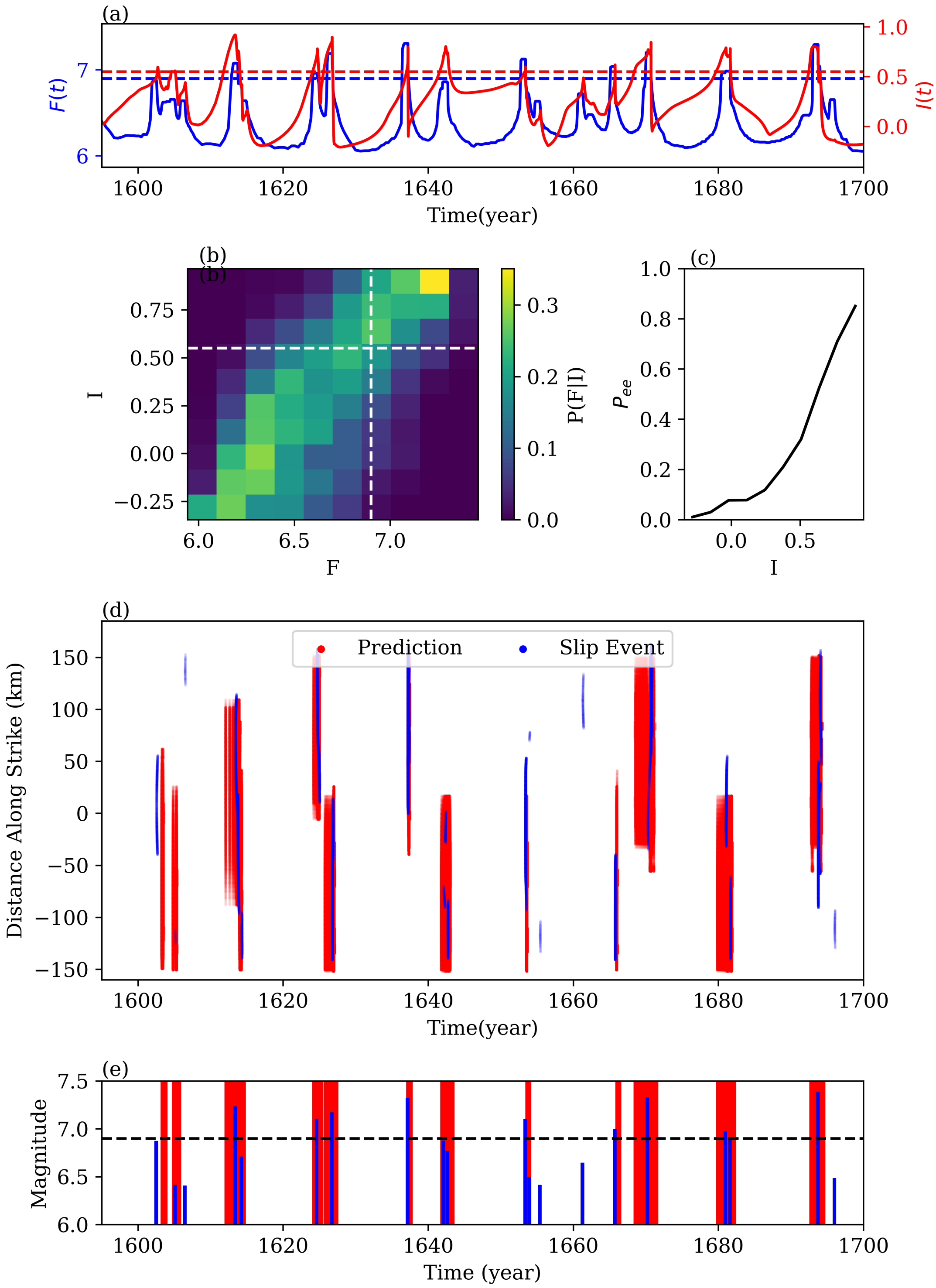

Figure 6. Spatio-temporal prediction of events same as in Fig 5 but using slip rate only at 16 points on the fault (denoted in Fig 1 (a) by diamonds)

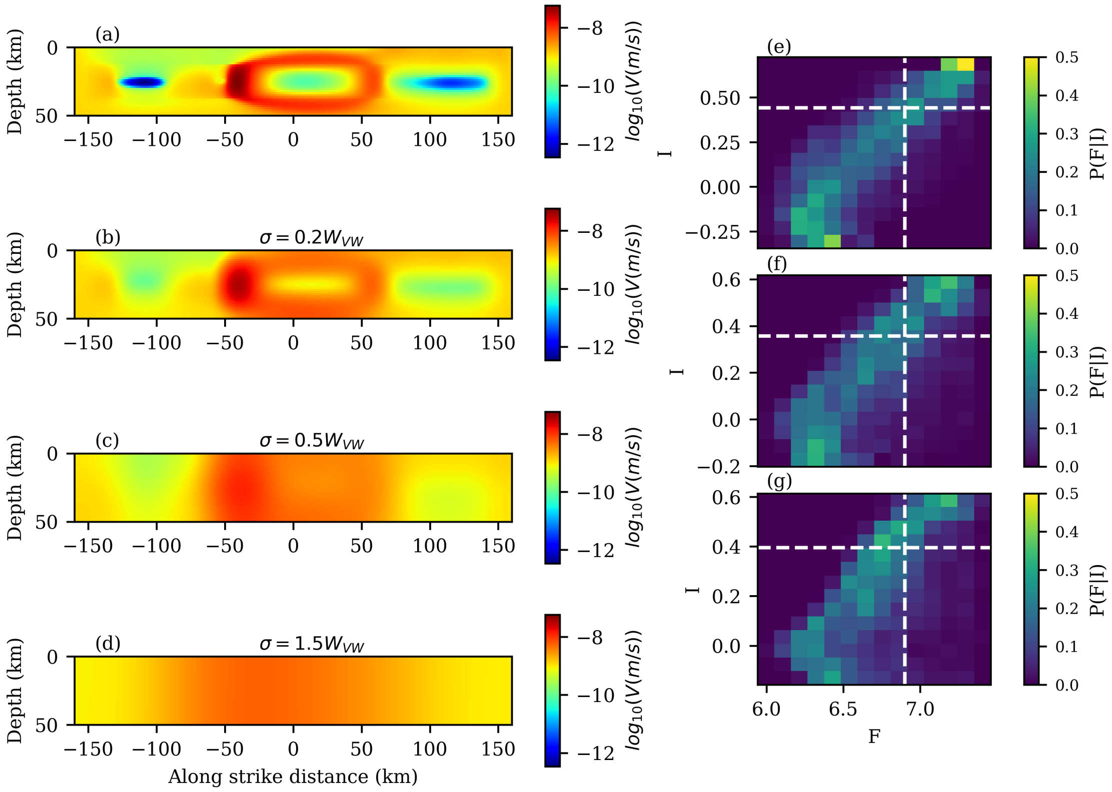

Figure 7. Impact of the low-pass filter noise on prediction. One snapshot of the slip rate is plotted in (a). To visualize the effect of noise, the low-pass filter applied to the snapshot in (a) is plotted in (b,c,d) with different standard deviations. The conditional probability of $P(F|I)$ when the slip rate is corrupted with a Gaussian low-pass filter with different noise standard deviations $(\sigma = 0.2W_{VW}, 0.5W_{VW}, 1.5W_{VW})$ are plotted in (e,f,g) respectively.

APPENDIX A: PROPER ORTHOGONAL DECOMPOSITION (POD): METHOD AND RESULT

In this section, we review how to reduce the dimension of the dataset consisting of slip rate and state variable using the POD method. We use this method to find critical prestress in a low-dimensional space instead of the high-dimensional function space. Another reason to use this method is because Eq (9) is an optimization problem constrained on the chaotic attractor of the system with the event period excluded. To solve the constraint optimization problem (Eq (9)), one method (Farazmand & Sapsis, 2017) is to exclude the extreme events from the chaotic attractor and approximate the remaining using the POD technique. Here, we exclude the event period from the dataset to only approximate the interevent period. The method of approximating the chaotic attractor using POD modes is used in different fields. As an example, the work in (Blonigan et al., 2019) used 50 POD modes to approximate the chaotic attractor of a turbulent channel flow. One behavioral difference between our model of the earthquake cycle and the turbulent channel flow example is that the time stepping in our problem is adaptive due to the system's multi-scale behavior; there are more sample data when the dynamical system is stiff. However, since we are removing the event period from the data, we only include the slow part of the system in our dataset.

In the following paragraphs, we describe the POD analysis on our dataset of simulations. The data set comprises snapshots within the time span from the year 200 to 1200 excluding the event set ($E(V_{\text{thresh}})$). We use the time snapshots of discretized states of the system (θ and V) which belong to a high but finite-dimensional space. After discretization, $V : \mathbb{R}^{N_x \times N_y} \times \mathbb{R}^+ \to \mathbb{R}^+$ and $\theta : \mathbb{R}^{N_x \times N_y} \times \mathbb{R}^+ \to \mathbb{R}^+$. $N_x = 256$ and $N_y = 32$ are the numbers of grid points along the strike and depth respectively.

Since the evolution of the system is better realized in $\log_{10}$ space, we apply the POD on the $\log_{10}$ of the dataset. We define vectors $w_1(t_k)$ and $w_2(t_k)$ both in $\mathbb{R}^{N_x N_z}$ for time t_k as the vectorized form of the logarithm of V and θ at time t_k.

$$w_1(t_k) = \log_{10} \left(\begin{bmatrix} V_{1,1} \\ V_{1,2} \\ \vdots \\ V_{1,N_x} \\ V_{2,1} \\ V_{2,2} \\ \vdots \\ V_{2,N_x} \\ \vdots \\ V_{N_z,1} \\ V_{N_z,2} \\ \vdots \\ V_{N_z,N_x} \end{bmatrix} \right)_{t=t_k} \tag{A.1}$$

$$w_2(t_k) = \log_{10} \left(\begin{bmatrix} \theta_{1,1} \\ \theta_{1,2} \\ \vdots \\ \theta_{1,N_x} \\ \theta_{2,1} \\ \theta_{2,2} \\ \vdots \\ \theta_{2,N_x} \\ \vdots \\ \theta_{N_z,1} \\ \theta_{N_z,2} \\ \vdots \\ \theta_{N_z,N_x} \end{bmatrix} \right)_{t=t_k} \tag{A.2}$$

where for example, by $[V_{i,j}]_{t_k}$, we mean slip rate at i^{th} element along strike and j^{th} element along the depth at k^{th} snapshots in the dataset. Then, we stack pairs of w_1 and w_2 to make a vector w:

$$w(t_k) = \begin{bmatrix} w_1(t_k) \\ w_2(t_k) \end{bmatrix} \in \mathbb{R}^{2N_xN_z}. \tag{A.3}$$

We define $\bar{w} = [\bar{w}^V, \bar{w}^\theta]^\top$ as the time average of $w(t_i)$ for all i in the dataset.

$$\bar{w} = \frac{1}{N_d} \sum_{i=1}^{N_d} w(t_i) \tag{A.4}$$

where N_d is the total number of snapshots in the dataset. $\bar{w}^V$ and $\bar{w}^\theta$ are plotted in Fig 3. We define $p(t_k) = w(t_k) - \bar{w}$ and then we define a matrix $P \in \mathbb{R}^{2N_xN_z \times N_d}$ with the following entries:

$$P = [p(t_1)\ p(t_2)\ \cdots\ p(t_{N_d})] \in \mathbb{R}^{2N_xN_z \times N_d}. \tag{A.5}$$

Then, we define the covariance matrix R as the following:

$$R = \frac{1}{(N_d - 1)} PP^T \in \mathbb{R}^{2N_xN_z \times 2N_xN_z} \tag{A.6}$$

Now, we can find the eigenvectors of matrix R:

$$R\phi_j = \lambda_j \phi_j \quad \lambda_1 \geq \lambda_2 \geq ... \geq \lambda_{2N_xN_z} \geq 0. \tag{A.7}$$

Eigenvalues show how well each eigenvector captures the original data in L^2 sense. Eigen-vectors of matrix R can be found using Singular Value Decomposition (SVD) of matrix P:

$$P = \Phi\Sigma\Psi^T \tag{A.8}$$

where in general $\Phi \in \mathbb{R}^{2N_xN_y \times 2N_xN_y}$ and $\Psi \in \mathbb{R}^{N_d \times N_d}$ are orthogonal ($\Phi\Phi^T = I_{2N_xN_y \times 2N_xN_y}$ and $\Psi\Psi^T = I_{N_d \times N_d}$) and determine, through columns, the left and right singular vectors of P; and diagonal matrix $\Sigma \in \mathbb{R}^{2N_xN_y \times N_d}$ has singular values on its diagonal (Taira et al., 2017). We can write:

$$R = \frac{1}{(N_d - 1)} PP^T = \frac{1}{(N_d - 1)} \Phi\Sigma\Psi^\top\Psi\Sigma^\top\Phi^\top$$

$$R\Phi = \frac{1}{(N_d - 1)} \Phi\Sigma\Sigma^\top \tag{A.9}$$

because of the special form of Σ that will be discussed shortly, the columns of Φ (denoted here by ϕ_i and are plotted in Fig 3 for $i \leq 4$) are eigenvectors of matrix R that are ordered by the variance they capture in data. Note that $\phi_i \in \mathbb{R}^{2N_xN_y}$ and we can separate it into eigenvectors of the slip rate (ϕ_i^V) and the state variable ϕ_i^θ:

$$\phi_i = \begin{bmatrix} \phi_i^V \\ \phi_i^\theta \end{bmatrix} \tag{A.10}$$

Assuming the number of time snapshots is much smaller than the dimension of the problem $N_d \ll 2N_xN_y$, Σ has the following form:

$$\Sigma = \begin{bmatrix} \sigma_1 & 0 & 0 & 0 \\ 0 & \sigma_2 & 0 & 0 \\ \vdots & \vdots & \ddots & \vdots \\ 0 & 0 & 0 & \sigma_{N_d} \\ 0 & 0 & 0 & 0 \\ \vdots & \vdots & \vdots & \vdots \\ 0 & 0 & 0 & 0 \end{bmatrix}_{2N_xN_y \times N_d} \tag{A.11}$$

Then, using Eqs (A.7), (A.9), and (A.11), $\frac{1}{(N_d-1)}\sigma_j^2 = \lambda_j$. λ_j corresponds to the variance of the data along ϕ_j. If λ_j goes to zero very fast, it suggests that we can explain the dataset in a low-dimensional subspace consisting of a finite number of eigenfunctions. The ratio $\sum_{j=1}^{r} \lambda_j / \sum_{j=1}^{N_d} \lambda_j$ shows the proportion of the variance of the data that are captured in the first r eigenfunctions. Based on Fig A1, the first 13 modes of the data capture almost 85% of the data.

Using this explanation, we can approximate the interevent period ($\mathcal{A} \setminus E(V_{\text{thresh}})$) by:

$$\log_{10}\left(\mathcal{A} \setminus E(V_{\text{thresh}})\right) \approx \Big\{ w = \bar{w} + \sum_{i=1}^{N_m} a_i\phi_i \Big| \sum_{i=1}^{N_m} \frac{a_i^2}{\lambda_i} \le r_0^2 \Big\}. \tag{A.12}$$

where N_m is the number of modes (eigenfunctions) that are considered in the truncation. One can play with r_0 to enlarge the set. For very large r_0 the approximation is not valid anymore. The value of r_0 determines how much we let perturbation around the average of the dataset $\bar{w}$. As an example, taking $N_m = 1$ and $r_0 = 1$ would let perturbation around $\bar{w}$ along ϕ_1 with an amplitude equal to the standard deviation of the dataset along that eigenvector ($\sqrt{\lambda_1}$).

Using the orthonormality of ϕ_i's, we can find the projection of any $w(t)$ onto ϕ_i using the following inner product:

$$a_i(t) = \langle w(t) - \bar{w}, \phi_i \rangle \tag{A.13}$$

where $a_i(t)$ is the projection of $w(t) - \bar{w}$ onto eigenvector ϕ_i and $<,>$ denotes the inner product. We can find $a_i(t_k)$ for all of the time snapshots in the dataset and plot the distribution of $a_i/\sqrt{\lambda_i}$ (Fig A2). We see that the distribution is close to the standard normal distribution. Looking at this figure gives us intuition about choosing a value for r_0. For example, selecting r_0 to be large (> 4), would lead to exploring low-probability regions. The dashed lines in the figure, correspond to $a_i/\sqrt{\lambda_i} = 1,\ 2,\ 3.$

Using the approximation in Eq (A.12), we reduce the dimensionality of the system from $\mathbb{R}^{2N_xN_z}$ to $\mathbb{R}^{N_m}$ and approximate a complicated set $(\mathcal{A} \setminus E(V_{\text{thresh}}))$ by a hyperellipse which is a straightforward constraint for our optimization problem. With the mentioned approximation, and denoting $w^* = \bar{w} + \sum_{i=1}^{N_m} a_i^* \phi_i$, we write an optimization problem in the low dimensional $\mathbb{R}^{N_m}$ space which is an equivalent approximate of Eq (9):

$$A^* = \{\mathbf{a}^* | \sum_{i=1}^{N_m} \frac{a_i^{*2}}{\lambda_i} \leq r_0^2,\ w^* \text{ is a local maximizer of } F(10^{w^*}; \Delta t, T), F(10^{w^*}; \Delta t, T) > F_e^*\} \tag{A.14}$$

where $\mathbf{a}^* \in \mathbb{R}^{N_m}$ whose i^{th} element is a_i^*. Eq (A.14) ensures that the optimal solutions are not too far from the mean states $(\bar{w})$.

To show the applicability of the POD model reduction outside the application of this paper, we also applied the method to a dataset including all snapshots within the period of 200 years to 1200 years (without removing the event period). The result of this model reduction is available in Supplemental Video 2. This video shows that we can capture all phases of earthquake cycles using a few POD modes.

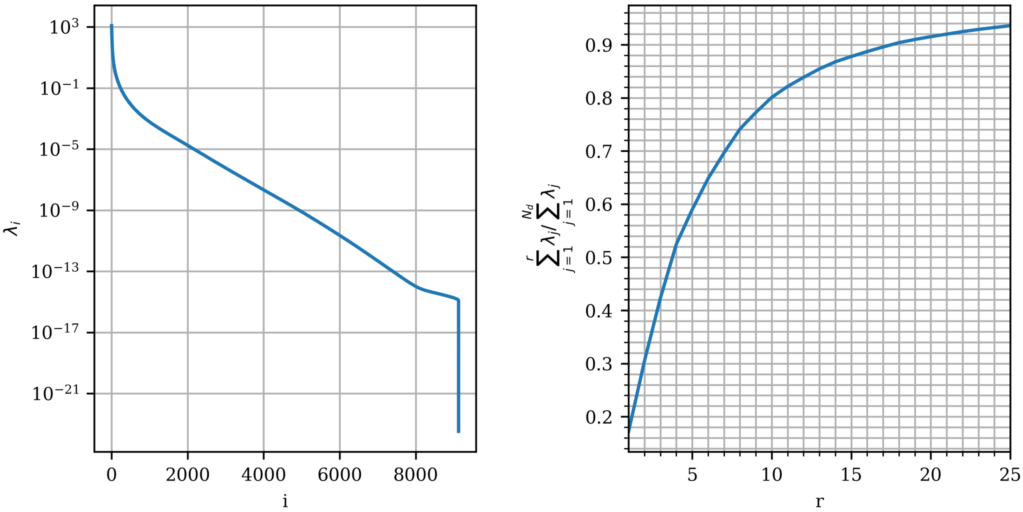

Figure A1. Convergence of the eigenvalues (left) and the ratio of a truncated sum of eigenvalues to the total sum of eigenvalues (right).

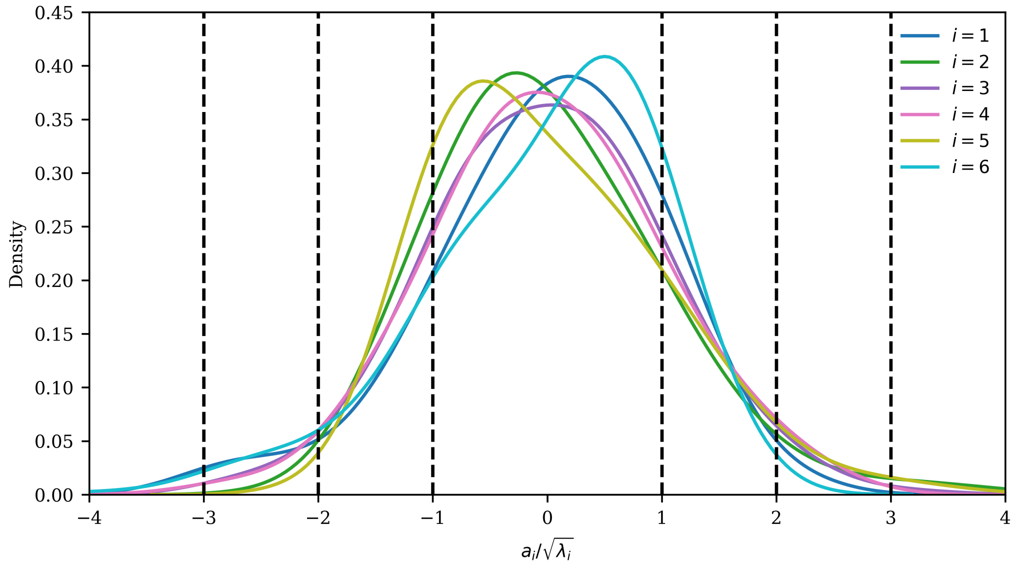

Figure A2. The distribution of $a_i(t)/\sqrt{\lambda_i}$ in the dataset of the interevent periods. The vertical lines correspond to $a_i/\sqrt{\lambda_i} = \pm 1,\ \pm 2,\ \pm 3$ and are plotted to give insight for selecting proper r_0 in Eq (10)

APPENDIX B: OPTIMIZATION

Here we revisit optimal sampling in the framework of Bayesian optimization as discussed in (Brochu et al., 2010) and is improved in (Blanchard & Sapsis, 2021) for finding the precursors of extreme events. The optimization algorithm works by exploring the input space ($\mathbf{a} = [a_1, ..., a_{N_m}] \in \mathbb{R}^{N_m}$) using a Gaussian surrogate model. Suppose that we want to solve the constrained optimization problem of Eq (9) with the approximation in Eq (10). Without loss of generality, we study the minimization of the minus sign of the cost function ($G = -F$) instead of maximizing it. The cost function can be evaluated using a forward simulation of a given initial condition. Here we assume that the observation is contaminated by a small Gaussian noise with variance $\sigma_\epsilon^2 = 10^{-4}$.

$$z = G(a; T, \Delta t) + \epsilon \quad \epsilon \sim \mathcal{N}(0, \sigma_\epsilon^2) \tag{B.1}$$

where ϵ is the observational noise, and T and Δt are hyperparameters of the cost function G that are determined before the optimization process. The iterative approach starts from some randomly sampled N_{init} points $\{\mathbf{a_k} \in \mathbb{R}^{N_m}\}_{k=1}^{N_{init}}$ that each of them corresponds to a point in the set defined in (10). Using the forward model of Eq (B.1) we find the input-output pair $\mathcal{D}_0 = \{\mathbf{a_k}, z_k\}_{k=1}^{n_{init}}$. $\mathbf{a_k} \in \mathbb{R}^{N_m}$ is the vector of POD coefficients with N_m as the number of POD modes we have decided to consider, and z_k comes from Eq (B.1). Using a Gaussian surrogate model, the expected value and variance of the process, condition on the input/output at each step i ($\mathcal{D}_i$) is given by the following equation:

$$\begin{aligned} \mu(\mathbf{a}) &= m_0 + k(\mathbf{a}, \mathbf{A}_i)\mathbf{K}_i^{-1}(\mathbf{z}_i - m_0) \\ \sigma^2(\mathbf{a}) &= k(\mathbf{a}, \mathbf{a}) - k(\mathbf{a}, \mathbf{A}_i)\mathbf{K}_i^{-1}k(\mathbf{A}_i, \mathbf{a}) \end{aligned} \tag{B.2}$$

where $\mathbf{K}_i = k(\mathbf{A}_i, \mathbf{A}_i) + \sigma_\epsilon^2\mathbf{I}$, $\mathbf{A}_i = \{\mathbf{a_k}\}_{k=1}^{N_{init}+i}$, and $\mathbf{z}_i = \{z_k\}_{k=1}^{N_{init}+i}$. We consider the Radial Basis Function (RBF) with Automatic Relevance Determination (ARD):

$$k(\mathbf{a}, \mathbf{a}') = \sigma_f^2 \exp(-(\mathbf{a} - \mathbf{a}')^T \Theta^{-1} (\mathbf{a} - \mathbf{a}')/2) \tag{B.3}$$

where Θ is a diagonal matrix containing the length scale for each dimension. At each iteration, we construct a surrogate model (Eq (B.2)). Then, the next point in the input space is found by minimizing an acquisition function ($g : \mathbb{R}^{N_m} \rightarrow \mathbb{R}$). We use the **Lower Confidence Bound** (LCB) acquisition function which is defined as the following:

$$g_{LCB}(\mathbf{a}) = \mu(\mathbf{a}) - \kappa\sigma(\mathbf{a}) \tag{B.4}$$

where κ is a positive number that balances exploration and exploitation. For small κ, we do not consider uncertainties of the surrogate model and trust the mean of the conditional Gaussian process. For large κ, minimizing Eq (B.4) is equivalent to finding a point that has the largest uncertainty. We use $\kappa = 1$ in this study. The algorithm is extracted from Ref (Blanchard & Sapsis, 2021) and is summarized in Algorithm 1. We start the algorithm by randomly sampling 10 initial points inside the hyper-ellipse (Eq (10)) and then augmenting the input-output pairs by minimizing the acquisition function until the size of the input-output points reaches 200. To show the effectiveness of the algorithm in finding optimal solutions, we define the function c as the following:

$$c(i) = -\min_{1\leq j\leq i} \min_{\mathbf{a}} \mu(\mathbf{a} \mid \mathcal{D}_j) \tag{B.5}$$

To find $c(i)$, we need to find the minimum of the Gaussian process in each iteration i and report the minimum over all $1 \leq j \leq i$. The algorithm does not guarantee finding all of the local maxima. As a result, the algorithm is repeated for 30 trials with different randomly chosen initial points. The behaviour of $c(i)$ for different values of r_0 is plotted in Fig B1 (a). The solid line is the median of $c(i)$ for different trials as a function of iteration and the shaded band shows half of the median absolute deviation. One of the optimal solutions is plotted in Fig B1 (b,c). During the optimization process, we augment the set W^* if the condition in Eq (11) is satisfied.

Algorithm 1 Bayesian Optimization

1: **Input:** Number of initial points n_{init} and number of iterations n_{iter}

2: **Initialize:** Surrogate model on initial dataset $\mathcal{D}_0 = \{\mathbf{a}^{(\mathbf{k})}, z^{(k)}\}_{k=1}^{n_{init}}$

3: **for** n=0 to n_{iter} **do**

4: Select best next point $\mathbf{a_{n+1}}$ by minimizing acquisition function constrained inside the hyperellipse (Eq (10)):

$$\mathbf{a^{(n+1)}} = \underset{\sum_{i=1}^{Nm} \frac{a_i^2}{\lambda_i} \le r_0^2}{\arg\min} \; g_{LCB}(\mathbf{a}; \bar{G}, \mathcal{D}_n)$$

5: Evaluate objective function G at $\mathbf{a^{(n+1)}}$ and record $z^{(n+1)}$

6: If $z^{(n+1)} < -F_e^*$ augment the set W^* (Eq (11))

7: Augment dataset $\mathcal{D}_{n+1} = \mathcal{D}_n \cup \{\mathbf{a_{n+1}}, z_{n+1}\}$

8: Update surrogate model

9: **end for**

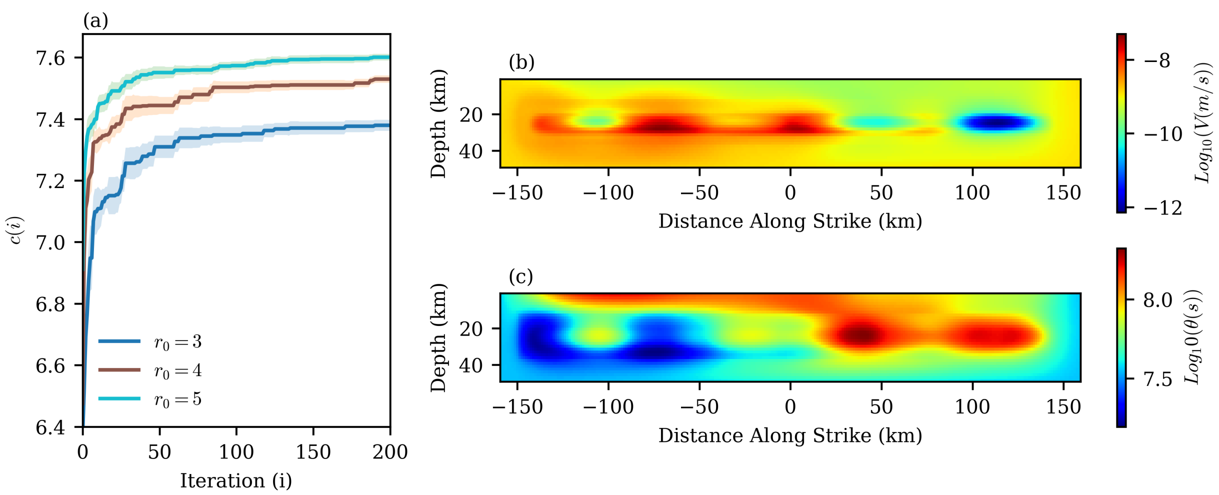

Figure B1. Convergence of the optimization for different values of r_0 (a). $\log_{10}(V)$ and $\log_{10}\theta$ of one of the optimal solutions with $r_0 = 3$ which leads to a magnitude 7.5. The optimal solution is highly heterogeneous and shows the effect of favorable stress heterogeneity in generating big events (b,c). The stress calculated from this optimal solution is plotted in Fig 4